

www.acsami.org Research Article

# Wafer-Scale Fabrication of Uniform, Micrometer-Sized, Triangular Membranes on Sapphire for High-Speed Protein Sensing in a Nanopore

Pengkun Xia, Md Ashiqur Rahman Laskar, and Chao Wang\*



Cite This: ACS Appl. Mater. Interfaces 2023, 15, 2656-2664



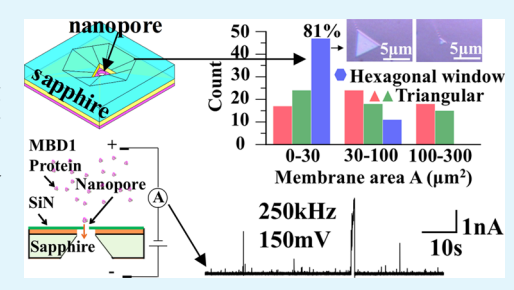
**ACCESS** I

Metrics & More

Article Recommendations

Supporting Information

ABSTRACT: Ultra-low-noise solid-state nanopores are attractive for high-accuracy single-molecule sensing. A conventional silicon platform introduces acute capacitive noise to the system, which seriously limits the recording bandwidth. Recently, we have demonstrated the creation of thin triangular membranes on an insulating crystal sapphire wafer to eliminate the parasitic device capacitance. Uniquely different from the previous triangular etching window designs, here hexagonal windows were explored to produce triangular membranes by aligning to the sapphire crystal within a large tolerance of alignment angles  $(10-35^{\circ})$ . Interestingly, sapphire facet competition serves to suppress the formation of more complex polygons but creates stable triangular membranes



with their area insensitive to the facet alignment. Accordingly, a new strategy was successfully established on a 2 in. sapphire wafer to produce chips with an average membrane side length of 4.7  $\mu$ m, an area of <30  $\mu$ m<sup>2</sup> for 81% chips, or estimated calculated membrane capacitance as low as 0.06 pF. We finally demonstrated <4  $\mu$ s high-speed and high-fidelity low-noise protein detection under 250 kHz high bandwidth.

KEYWORDS: wafer-scale fabrication, small membrane, low noise, low capacitance, high bandwidth, sapphire etching, protein sensing

#### 1. INTRODUCTION

Solid-state nanopore have great potential to be a portable, lowcost, and versatile single-molecular biosensor. 1-3 However, it remains a challenge to design and fabricate low-noise nanopore devices. One major challenge in using prevalent crystalline silicon as the support substrate is the acute capacitive noise due to its conductivity, especially at high recording frequencies. The chip capacitance  $(C_{\text{chip}})$  typically has to be mitigated to <100 pF by using elastomer painting,<sup>4,5</sup> a thick dielectric film, 6,7 or high-resistivity silicon for general low-noise use. Efforts to reduce the  $C_{chip}$  to sub 10 pF for high-accuracy sensing usually have to incorporate a thick dielectric film, painting insulating layers, and electron-beam lithography (EBL) together, 9,10 preventing low-cost and large-scale manufacturing. Glass, as a highly resistive material, has demonstrated excellent performance in eliminating the stray capacitance  $(C_s)$  and reducing the total  $C_{\rm chip}$  down to a few pico farads. Nonetheless, more economic acid-based isotropic glass etching is not feasible to achieve desired precise dimensional control, which is necessary for producing a small membrane area (A) and small membrane capacitance ( $C_{\rm m} \propto$ A). 14 EBL-involved stepwise etching and femtosecond laserassisted etching were demonstrated to successfully control the membrane area, but precise size control remains elusive (e.g., a large range from 20 to 1200  $\mu$ m<sup>2</sup> was reported), <sup>12,13,15</sup> and the processes are comparatively more complex and expensive.

Recently, we demonstrated a novel approach to creating thin triangular nanopore membranes on an insulating crystal sapphire wafer to completely eliminate  $C_s$  of the device. i6 In particular, a triangular-shaped window was used to define a cavity in sapphire in wet etching, eventually etching through the sapphire and suspending a dielectric (e.g., silicon nitride or SiN<sub>x</sub>) membrane. By aligning the etching windows to the sapphire A-plane (11 $\overline{20}$ ) within a specific angle range (e.g.,  $40^{\circ}$ in our work 16), the membranes were formed in a triangular geometry. This process enabled 2 in. wafer-scale fabrication of suspended dielectric membranes by inexpensive batchprocessing-compatible wet etching for the first time. In this study, we present a new approach to creating triangular membranes, defined not by triangular etching windows but by hexagonal window designs. Interestingly, the triangular membrane dimension is much less sensitive to the window alignment to the sapphire crystal, showing a relative standard deviation (RSD) of the membrane area as small as 4.5% within a wide range of mask alignment angles ( $10^{\circ} < \alpha < 35^{\circ}$ ). The

Received: October 21, 2022 Accepted: December 21, 2022 Published: January 4, 2023





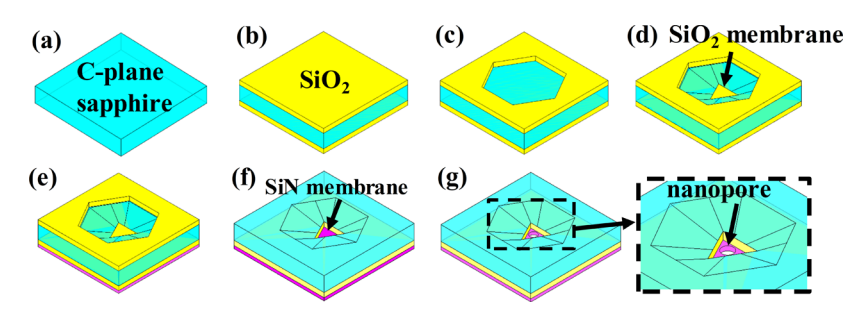


Figure 1. Key steps of nanopore fabrication on sapphire using a hexagonal etching mask design. (a) A 250  $\mu$ m sapphire wafer is cleaned with solvents and RCA2. (b) A layer of PECVD SiO<sub>2</sub> (~1  $\mu$ m) with excellent etching selectivity over the sapphire (~1:1000 in this work) was deposited on both sides of the sapphire wafer. (c) A hexagonal-shaped window is formed in the top SiO<sub>2</sub> by photolithography and RIE. (d) The sapphire is etched through in hot sulfuric acid and phosphoric acid, forming a suspended SiO<sub>2</sub> membrane. (e) A thin layer of LPCVD SiN is deposited on the bottom SiO<sub>2</sub> membrane, and unintentionally deposited SiN in the cavity is etched by RIE. (f) The thin SiN membrane is formed by first selectively removing the SiO<sub>2</sub> membrane with HF acid and then optionally thinning SiN in hot phosphoric acid. (g) A nanopore is drilled by a transmission electron microscope in the SiN membrane.

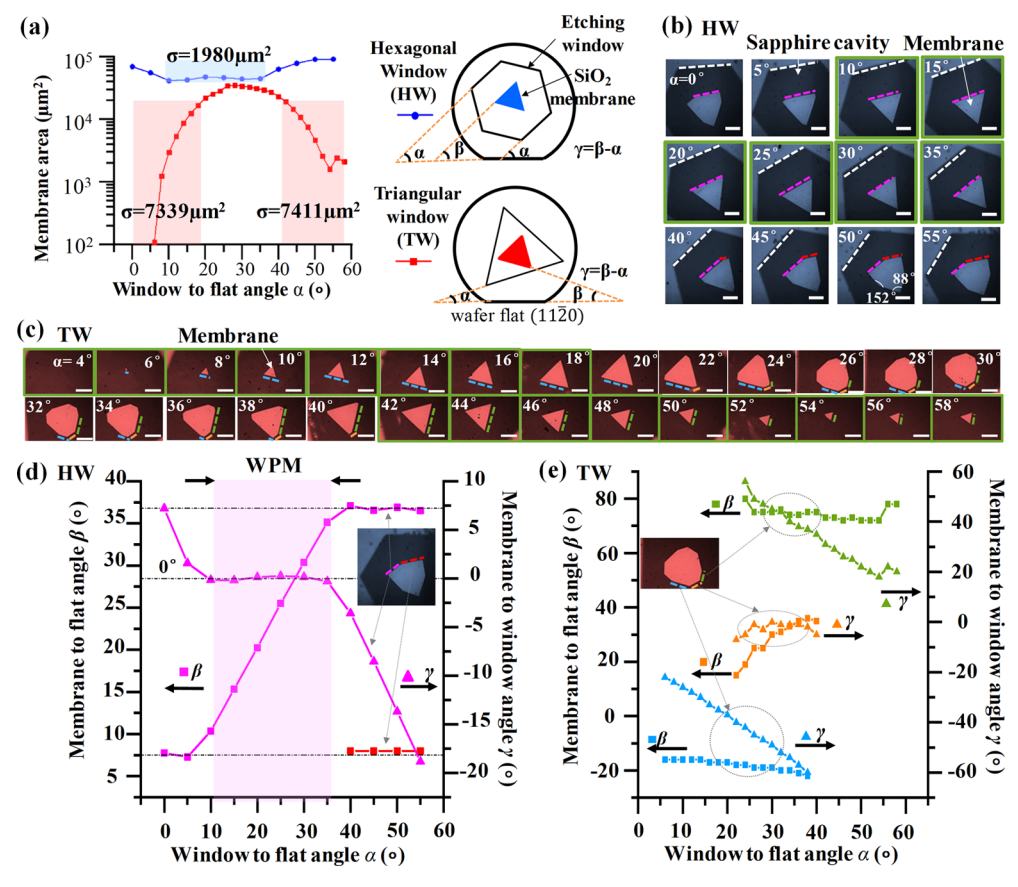


Figure 2. Dependence of the membrane geometry on the window-to-sapphire-crystal alignment for hexagonal and triangular window mask designs. (a) Experimental study comparing the hexagonal window (blue) and the triangular window (red) mask design on the  $SiO_2$  membrane area affected by the alignment offset angle  $(\alpha)$ , the window side to the sapphire wafer flat) after the sapphire etching. The angle range of  $\alpha$  to form equilateral triangular membranes is shadowed. The right-side two schematics show the angle  $\alpha$ , membrane to flat angle  $\beta$ , and membrane to window angle  $\gamma$  for hexagonal and triangular window designs, respectively. (b,c) Optical images of the formed  $SiO_2$  membranes on a sapphire wafer with (b) hexagonal window masks and (c) triangular window masks as  $\alpha$  changes from 0 to  $<60^{\circ}$ . The images corresponding to equilateral triangular membranes are green-outlined. The white dashed lines are used to highlight the hexagonal window sides parallel to the membranes ( $10^{\circ} < \alpha < 35^{\circ}$ ). The hexagonal window side length  $L_1$  is  $500 \ \mu\text{m}$ , and the sapphire etching depth is  $232 \ \mu\text{m}$  (not fully etched). The scale bar is  $100 \ \mu\text{m}$  for both (b,c). (d,e) Membrane side orientation relative to the wafer flat (left  $\gamma$ -axis,  $\beta$ , solid squares) and window sides (right  $\gamma$ -axis,  $\gamma$ , triangles) as  $\alpha$  changes from 0 to  $55^{\circ}$  or 4 to  $58^{\circ}$  for (d) hexagonal and (e) triangular window mask designs. The membrane is outlined and color-coded in (b) (magenta for triangular sides, red for additional sides in ditrigonal geometry) and (c) (blue and green for two different sets of triangular sides, and orange for the additional sides in the nonagonal geometry) for calculating  $\beta$  and  $\gamma$  angles in (d,e), respectively. (c) and part of (a) were reproduced with permission from © 2021 Elsevier.

design demonstrated uniform wafer-scale membrane patterning (81% membranes with area <30  $\mu m^2$  and 100% membranes

<100  $\mu m^2$ ) and excellent reproducibility (<3  $\mu m$  dimension deviation) from wafer to wafer. This new approach could

advance the low-noise and manufacturable solid-state nanopores for high-speed single-molecule sensing, demonstrated by low-noise protein detection at 250 kHz bandwidth using the SaS nanopore.

#### 2. RESULTS AND DISCUSSION

2.1. Hexagonal Etching Window Designs for Membrane Fabrication. Briefly, a hexagonal-shaped window was formed in a plasma-enhanced chemical vapor deposition (PECVD) silicon dioxide (SiO<sub>2</sub>) film on a c-plane sapphire (Figure 1a-c), and a batch-processing-compatible sapphire etching in concentrated sulfuric and phosphoric acids anisotropically etched sapphire to form a cavity and suspended membrane (Figure 1d). Then, the low-stress low-pressure chemical vapor deposition (LPCVD) silicon nitride (SiN) film was deposited on the suspended SiO<sub>2</sub> membranes. The unintentionally deposited SiN layer was removed via dry etching from the cavity side (not shown), and subsequently, the SiO<sub>2</sub> film was removed using HF-based wet etching to form the SiN membrane (Figure 1f), where the nanopores were drilled via a transmission electron microscope (Figure 1g).16 Here, the other side of the wafer was also coated with PECVD SiO<sub>2</sub> (Figure 1b) as the supporting membrane for the SiN membrane deposition (Figure 1e) after the sapphire etching (Figure 1d) as SiN could be easily removed by the phosphoric acid in the sapphire etching.

2.2. Membrane Geometry Control by the Etching Window Layout. The anisotropic sapphire etching is known to produce complex geometries, depending on the competition of different sapphire crystal facets during anisotropic wet etching, which is strongly affected by the etching window layout. For example, it was found that using the circular mask layout, only ditrigonal membranes were formed (Figure S1), which is consistent with the equatorial outline of the ditrigonal scalenohedron, known as the crystal lattice structure class for sapphire. 18,19 Differently, triangular etching windows produced membranes of different geometries, including nonagonal, ditrigonal, and triangular shapes, depending on the relative alignment between the etching mask and the sapphire crystal plane (Figure 2c).<sup>16</sup> Yet, the membrane geometry and area were rather sensitive to the alignment angle  $\alpha$  between the triangular mask and the c-plane sapphire wafer flat [A-plane, (1120)] (Figure 2a). <sup>16</sup> As a result, an error in  $\alpha$ , which is inevitable in practice, would result in a deviation in membrane size and adversely affect the accuracy of controlling the device capacitance. Such an effect makes it challenging to create reproducible small membranes.

To solve this problem, considering both the threefold symmetry of the sapphire crystal and its hexagonal structural unit cell, in this work, we devised hexagonal etching windows rather than triangular shapes. Interestingly, equilateral triangular membranes were produced with  $10^{\circ} \le \alpha \le 35^{\circ}$ and ditrigonal (irregular hexagonal) membranes with interior angles of 152 and 88° were formed for other  $\alpha$  angles (Figure 2b), but nonagonal shapes were never revealed. This observation indicated that the hexagonal etching windows significantly differentiate from circular or triangular window layouts by posing different etching constraints. Intuitively, it can be understood that the anisotropic sapphire etching favors evolution into 6 n- and 3 r-plane facets, attributed to their slower etching rates (e.g., etching with circular pillars, <sup>20</sup>Figure S2). These *n*- and *r*-facets would create nonagons when intersecting with a c-plane sapphire (Figures S3-4). We

further hypothesize that such a ditrigonal shape might be derived from the intersection of the *c*-plane with three *n*-plane and three r-plane facets, with another three n-planes being suppressed during cavity formation (Figure S5a,b). Indeed, the interior angles of the theoretically derived ditrigon using the nonagon model are calculated as 150 and 90° (Figure S6), very close to that of the measured values from hexagonal windows (152 and 88°) (Figure S5b) and that of circular windows (159 and 81°) (Figure S5d). Such a small deviation could be attributed to the evolution of more complex planes from the rplane (Figure S5c,d). Additionally, such a ditrigonal profile [six bottom (6B) planes with interior angles of 152 and 88° was also observed using circular pillar masks (Figure S2), with facet indices identified as  $\{3\overline{4}17\}^{\frac{1}{20}}$  Our experiment showed that, as the etching window alignment angle  $\alpha$  changes, three of the six facets forming the ditrigonal crystal became suppressed, shortening their side lengths and eventually eliminating them to form triangular membranes (Figures 2b and S7). Noticeably, as  $\alpha$  changes, the interior angles of the nonagonal membranes deviated from the theoretical values by 5-16° (Figure S4a,b), again indicating the creation of more complex but *n*- and *r*-like planes (similar to 6B planes).

By analyzing the membrane geometry and area at different alignment angles  $\alpha$ , importantly, we discovered that the RSD of the membrane area of the formed triangular membranes  $(10^{\circ} \le \alpha \le 35^{\circ})$  by a hexagonal window mask is as small as 4.5% (44375  $\pm$  4.5%  $\mu$ m<sup>2</sup>), with a standard deviation ( $\sigma$ ) of 1980  $\mu$ m<sup>2</sup> (Figure 2a). These values are about 20 times smaller compared to the triangular window design  $[5715 \pm 83.9\% \ \mu m^2]$  $(\sigma = 6813 \ \mu\text{m}^2)$  for  $6^{\circ} \le \alpha \le 18^{\circ}$ ;  $5940 \pm 81.7\% \ \mu\text{m}^2$   $(\sigma =$ 7275  $\mu$ m<sup>2</sup>) for 42°  $\leq \alpha \leq$  58°], <sup>16</sup> indicating a uniquely widerange layout design tolerance in crystal alignment where the membrane area remained almost constant. Besides, sapphire etching involves many slow-etch-rate crystal planes,<sup>21</sup> which is very different from conventional silicon alkaline micromachining, where the final etched profile is mainly determined by a single slow-etch-rate (111) plane.<sup>22</sup> This makes the etched profile in sapphire pretty complex and not only associated with the sapphire crystal plane but also significantly affected by the mask alignment. Here, within this unique design regime ( $\alpha$ from 10 to 35°), the formed triangular membrane sides were parallel to that of the hexagonal etching window instead of staying at a constant crystal plane, yielding a membranewindow angle offset  $\gamma \sim 0^{\circ}$  (Figure 2d, shadowed regime, denoted as MPW triangle). This indicates that multiple slowetch-rate sapphire crystal planes were involved and the mask alignment strongly impacts the etched profile within this alignment angle range. In comparison, within the ditrigonal regime (Figure 2d, unshadowed,  $\alpha = 0-5^{\circ}$  and  $40-55^{\circ}$ ), the membrane sides offset with the sapphire wafer flat by an angle  $\beta$  with fixed values ( $\beta \sim 8^{\circ}$  for  $\alpha = 0-5^{\circ}$  and  $\beta \sim 37^{\circ}$  for  $\alpha =$ 40-55°). Meanwhile, the interior angles of the ditrigonal membranes were found to be ~88 and ~152° (Figure 2b), indicating that the facet evolution is mainly dependent on the sapphire crystal but not the etching window layout, consistent with the formation of r- and n-like facets (e.g., 6B planes) that contributed to the creation of the ditrigonal membranes. Noticeably, such WPM phenomena were not observed when using the triangular window layout. For example, the values of  $\beta$  were almost constant (-16 and ~76°) with a ~90° offset when two distinct sets of triangular membranes (blue and green lines in Figure 2c,e) formed within angle ranges of  $0^{\circ} \leq$  $\alpha \le 20^{\circ}$  and  $40^{\circ} \le \alpha \le 60^{\circ}$ , and the values of  $\gamma$  linearly

changed with  $\alpha$ . The change of  $\beta$  and  $\gamma$  values in the nonagonal membrane geometry (20° <  $\alpha$  < 42°) was less regulated, possibly attributed to the fact that the nonagonal geometry is a transitional state between the two sets of triangles. This comparison between triangular and hexagonal windows indicates that the hexagonal window design imposed strong facet etching constraints to produce triangular WPMs that the triangular window design was not able to control.

We performed additional scanning electron microscopic (SEM) analysis to understand the complex facet competition that is expected to significantly affect the evolution of triangular and hexagonal membranes. In total, we observed six types of facets (F1–F6) in the cavity with  $\alpha = 55^{\circ}$  (Figure S8). For example, facets F4 and F5 intersect on the membrane to form a ditrigonal membrane with interior angles of 152 and 88° and rotational threefold symmetry, indicating that the F4 and F5 planes may be 6B-like ({3417}).20 Noticeably, 6B planes were reported as 57.3° offset to the c-plane in SEM measurement, very close to the *r*-plane  $(57.6^{\circ})$  and *n*-plane  $(61.2^{\circ})$  offset to the c-plane. This is consistent with our above hypothesis that the ditrigonal membranes emerged from the six r-like and n-like planes. Clearly, at a large  $\alpha$  angle  $(\sim55^{\circ})$ , multiple facets intercept the c-plane, thus forming ditrigons with similar side lengths. At a smaller  $\alpha$  (Figure S8b– f), the F3 and F4 evolution was suppressed, while F5 and F6 planes continued to enlarge and eventually merged into a single set of facets (F7) that intercept the c-plane of sapphire with equal side lengths (Figure S8c-f). By tilting the SEM stage, we roughly measured the slope angle (about  $\pm 2^{\circ}$  error) of all the facets for the design of  $\alpha = 25^{\circ}$  and  $55^{\circ}$  (Table S1). Accordingly, Miller-Bravais indices {hkil} of the exposed sapphire facets in the cavity were calculated by building a hexagonal coordinate system (Figure S9, Table S2). As expected, the calculated indices cannot be directly linked to any of the typical crystallographic planes of sapphire.<sup>21</sup> This validated the fact that sapphire etching involves many slowetch-rate planes. The above analyses presented the complex evolution of sapphire facets, which have been well documented with different etching mask layouts such as cavity<sup>23</sup> and pyramids, 20,24 attributed to its trigonal crystal and strong etching selectivity between the sapphire crystal planes.<sup>21</sup>

**2.3.** Membrane Size Design and Fabrication Reproducibility. Uniquely, the use of the hexagonal window allowed us to establish a theoretical design model to precisely control the membrane size (Figure 3b–c). Briefly, from the top view (Figure 3b), the window and membrane side lengths  $L_1$  and  $L_2$  are related to  $d_1$  and  $d_2$  as  $d_1 = \frac{\sqrt{3}}{2}L_1$  and  $d_2 = \frac{1}{2\sqrt{3}}L_2$ . Moreover, from the cross-sectional view (Figure 3c), the wafer thickness (~250  $\mu$ m in this work)

$$h = \tan \theta \times (d_1 - d_2) = \left(\frac{\sqrt{3}}{2}L_1 - \frac{1}{2\sqrt{3}}L_2\right)$$

where  $\theta$  is the slope angle of the single facet (F7).

Empirically, we built a model ( $\theta = 36.37^{\circ}$ ) using a single membrane on a test wafer to predict the membrane sizes (red curve, Figure 3d-e). Experimentally, we measured the membrane sizes from two wafers of different window size ranges, that is, 380–450  $\mu$ m for wafer A (black symbols and lines) and 393–415  $\mu$ m for wafer B (green symbols and lines). Noticeably, an average of only  $\pm 6~\mu$ m membrane size prediction accuracy was determined for a wide range of

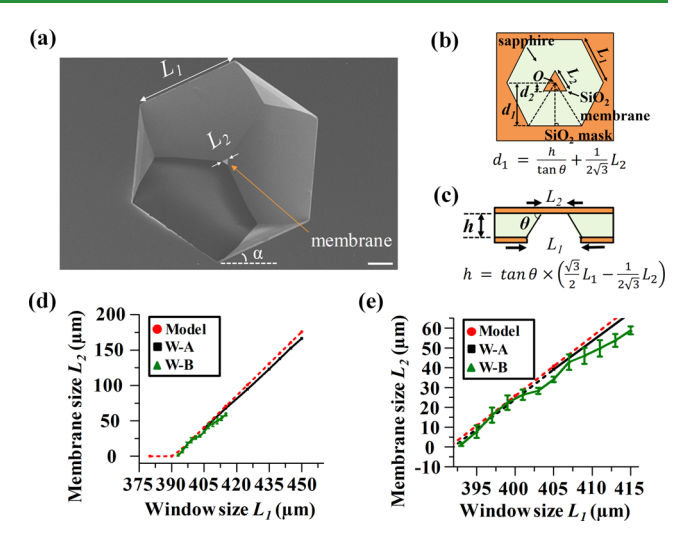


Figure 3. Membrane size prediction for the hexagonal window mask. (a) SEM image showing the sapphire facets in the cavity and WPM formation.  $\alpha=25^\circ$ . Scale bar: 100  $\mu$ m. (b,c) Top-view (top) and sideview (bottom) schematic of a sapphire chip.  $L_1$  and  $L_2$  are the window and membrane side lengths, respectively.  $\theta$  is defined as the effective facet angle relative to the c-plane after etching, here specifically the slope angle of F7. h is the sapphire wafer thickness. O is the central point of the triangular membrane and the hexagonal mask.  $d_1$  and  $d_2$  are the distance from point O to the window and membrane sides, respectively. (d) Correlation of SiO $_2$  membrane size with window size. Red curve: A model ( $\theta=36.37^\circ$ ) built using a single membrane ( $\alpha=25^\circ$ ) on a test wafer to predict the membrane sizes. Black curve: Experimentally produced membrane sizes (Wafer A: W-A). Green curve: Experimentally produced 214 membranes across a 2" wafer (Wafer B: W-B). (e) Zoomed view of (d) with  $L_1$  from 393 to 415  $\mu$ m.

membrane sizes (from 39 to 166  $\mu$ m) (Wafer A). With even smaller window designs (average size 403  $\mu$ m, Wafer B), the reproducibility deviation from Wafer A was as good as  $\pm 2.8$   $\mu$ m on average. Such consistency between experimentally determined and modeled membrane sizes clearly demonstrates great control in producing small membranes of single-digit micrometer sizes.

2.4. Uniform Patterning of <30  $\mu$ m<sup>2</sup> Triangular Membranes on a 2 in. Sapphire Wafer by Hexagonal Window Masks. We have analyzed the membrane size variations using both triangular and hexagonal etching mask designs (Figure 2a). Clearly, the use of a hexagonal window layout has the advantage to minimize the membrane size variation. Through engineering the dimension of the hexagonal window mask, we demonstrated a uniform patterning of 58 membranes over a 2 in. wafer (97% yield, in total 60 windows with two not forming membranes, Figure 4a). The average area was 16  $\mu$ m<sup>2</sup> and the majority (81%) was <30  $\mu$ m<sup>2</sup> (Figures 4d and S11), which was sufficient to effectively mitigate the  $C_m$  to a small value (0.06 pF estimated for a 30 nm thick membrane) that is insignificant given the presence of capacitance contribution from the measurement electronics (typically 5-20 pF).<sup>25</sup> Furthermore, compared to our previous triangular window design,16 the hexagonal windows also yielded more small membranes (Figure 4d) with reduced size deviation (Figure S11). For example, the number of small membranes (threshold defined as  $<30 \mu m^2$ ) doubled on the 2" sapphire wafer without any membranes over 100  $\mu$ m<sup>2</sup>, whereas about 30% of membranes were >100  $\mu$ m<sup>2</sup> in a triangular window design (Figure 4d). This analysis indicates that the hexagonal

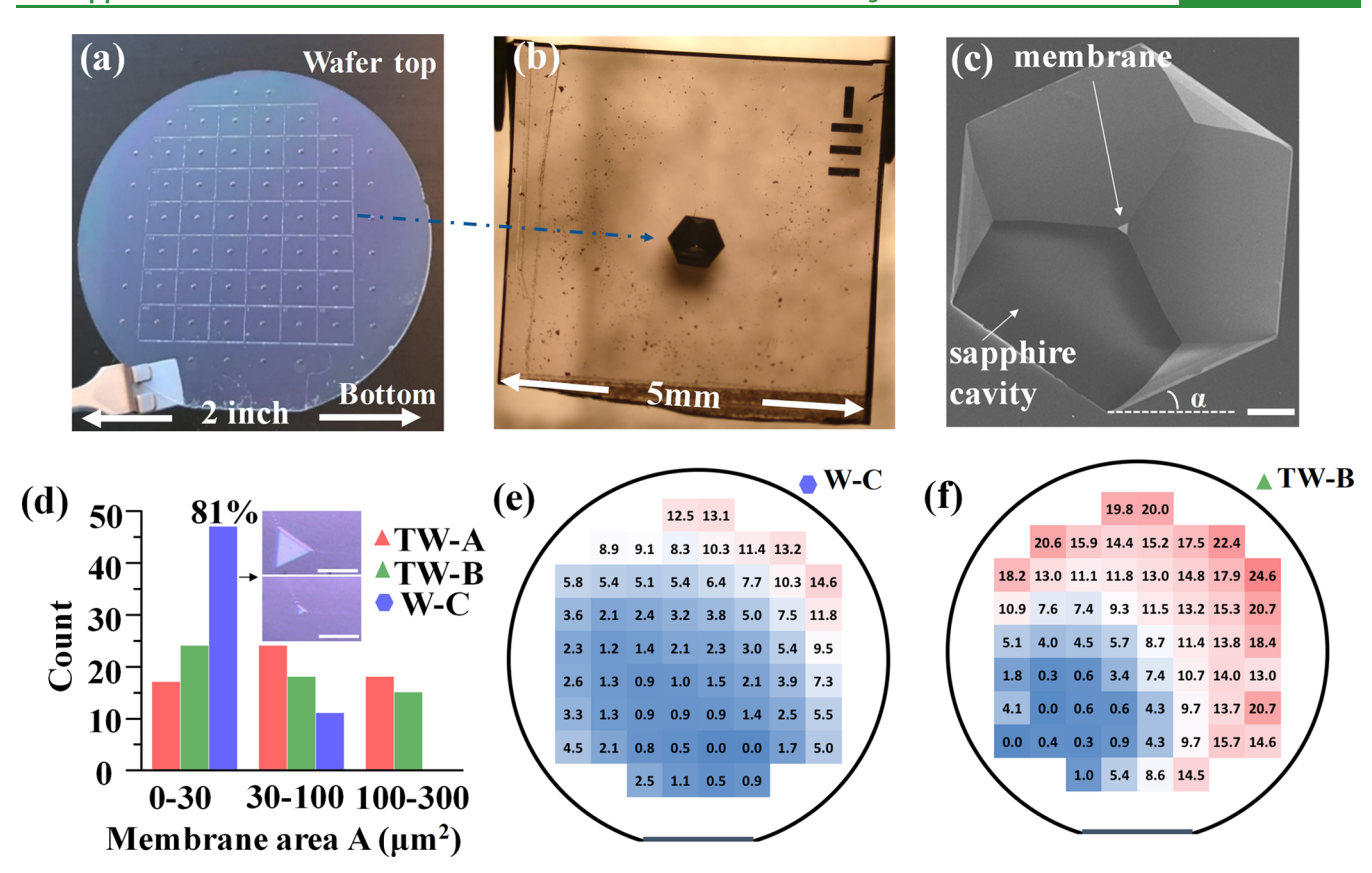


Figure 4. Uniform patterning of small triangular membranes on a 2 in. sapphire wafer by hexagonal window masks. (a) Optical image of a 2 in. sapphire wafer with intact, wafer-scale, small SiO<sub>2</sub> membranes with hexagonal window masks. (b) Optical image of a 5 mm by 5 mm sapphire chip diced from a 2 in. wafer. (c) SEM image showing the hexagonal window mask with the SiO<sub>2</sub> membrane in the center. Scale bar:  $100 \, \mu m$ .  $\alpha = 25^{\circ}$  ( $\alpha$ : the alignment angle between the etching window and the sapphire wafer flat A-plane ( $11\overline{20}$ )). (d) Wafer-scale small SiO<sub>2</sub> membrane distributions created from hexagonal windows (Wafer C, blue) and triangular windows (TW-D, red; TW-E, green). The insets show optical images of a  $0.6 \, \mu m^2$  and a  $12.6 \, \mu m^2$  SiO<sub>2</sub> membrane on Wafer C (scale bar:  $5 \, \mu m$ ). (e–f) Heat maps showing the membrane side lengths and membrane area on Wafer C.

mask design can greatly improve the yield of the small membranes.

2.5. Membrane Size Uniformity Study. To study the factors affecting the membrane dimension uniformity across the wafer, we plotted the membrane side length  $L_2$  as a heat map on the 2" wafer schematic (Figure 4e). First, we found that  $L_2$  decreases continuously from one side of the wafer (top) to another (bottom). This may be attributed to the higher temperature or stronger acid agitation at the bottom of the acid, and the top part of the wafer sitting at the bottom of the boat during sapphire etching. Second, another source of error could be the wafer thickness variation (Figure S14), which would eventually contribute to membrane dimension variation. It is observed that  $L_2$  tends to decrease from the wafer edge toward the wafer center (Figure 4e). Speculating that the wafer thickness variation could play a role (Figure S14b,d), we designed a radially rotating and pie-shaped layout with 13 slices on a 2 in. wafer, varying  $L_1$  from 391 to 415  $\mu$ m (Figure S15a). Each slice had the same  $L_1$  dimension with 16– 19 windows. The windows were located at different radii [from  $d_1$  (2.5 mm to the wafer edge) to  $d_8$  (8 × 2.5 mm to the wafer edge)]. Each  $L_2$  in Figure S15a is averaged from one to three membranes within the same slice (or  $L_1$ ) and at the same radius (or  $d_i$ ). Clearly, the membranes formed on the wafer center were in general smaller than those on the wafer edge (Figures S15b, 4e-f and S14). Given a step size of 2.5 mm in

radius (from  $d_2$  to  $d_8$ ), the corresponding  $L_2$  has a 1.0–1.8  $\mu$ m dimension reduction on average (Figure S15c). We also noticed a much more linear dependence of these small membrane sizes on the window sizes when the windows were placed >5 mm away from the edges (Figure S16). For example, the Pearson correlation coefficient (Pearson's r), used to measure the linearity between two sets of data, was improved by  $\sim$ 0.02 to 0.987 with i increasing from 1 to 2 but maintained above 0.994 with i = 4 to 8. The worse linearity at the very edge can be attributed to the wafer thickness variation, the local difference in acid temperature and agitation, etc.

**2.6. Ionic Current Noise Characterization.** With intact small suspended SiO<sub>2</sub> membranes formed on the sapphire, a layer of LPCVD SiN film was deposited onto the SiO<sub>2</sub> membrane. The unintentionally deposited SiN deposited at the sapphire cavity side was removed by brief RIE etching. Then, SiO<sub>2</sub> within the cavity was removed by HF to suspend the SiN membrane. Finally, the SiN membrane could be thinned down to desired thickness by phosphoric acid etching (30 nm thick in this study), and a nanopore was created via transmission electron microscopy (TEM) drilling (Figure 1e–g and Figure S17). The root-mean-square (RMS) current noise of the sapphire chip is as low as 43 pA under 250 kHz high bandwidth, that is, 3 times smaller than a typical 269 pF silicon-supported (SiS) nanopore (Figure S18a). By performing the ionic current noise analysis, we observed that the SaS

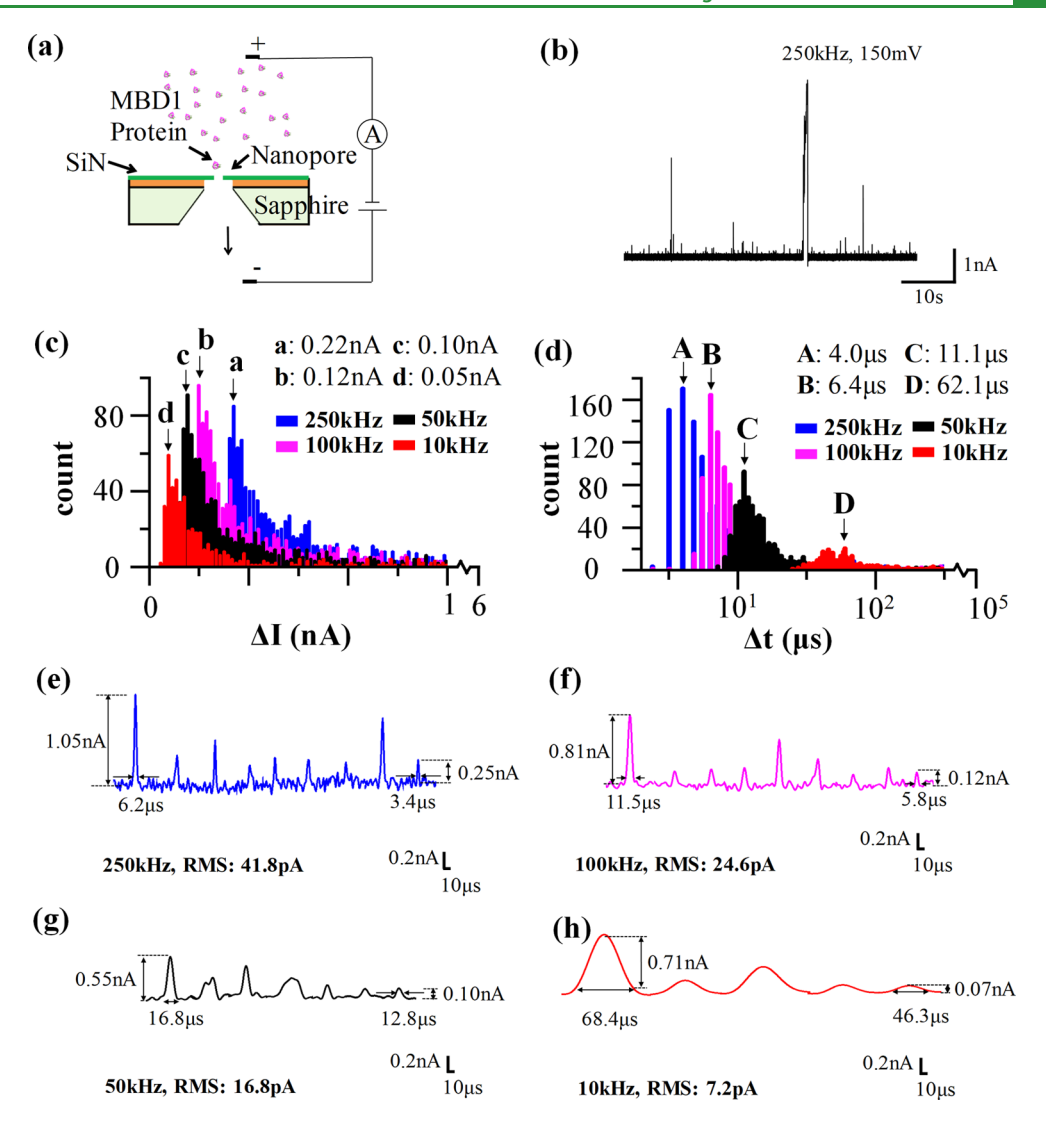


Figure 5. High-speed, low-noise protein sensing by SaS nanopores under a high bandwidth. (a) Schematic showing the translocation of the MBD1 protein through a SaS nanopore. Membrane side length:  $\sim$ 40 μm. (b) Current traces of the MBD1 protein translocation events in a SaS nanopore under 250 kHz and 150 mV ( $\sim$ 20 nM MBD1 concentration). The proteins are positively charged, so negative potential was applied for protein translocation and the signals are upward. (c) Histograms of Δ*I* for all four bandwidths. The 250, 100, 50, and 10 kHz bandwidths present a peak value (modal value in the histogram) of about 0.22, 0.12, 0.10, and 0.05 nA, respectively. (d) Histograms of Δ*t* for all four bandwidths. The 250, 100, 50, and 10 kHz bandwidths present a peak value (modal value in the histogram) of about 4.0, 6.4 μs, 11.1 μs, and 62.1 μs, respectively. (e–h) Representative current events under the 250, 100, 50, and 10 kHz bandwidth, respectively.

nanopores demonstrated 1 order of magnitude smaller spectral power density (PSD) than the SiS nanopore at a high bandwidth regime (Figure S18b), suggesting dramatically reduced capacitive noise. For SaS nanopores with parasitic capacitance completely eliminated, further reduction in the membrane area from 275 to 32  $\mu$ m<sup>2</sup> did not present a significant difference in chip capacitance and current noise (Figure S18). Nevertheless, the chip capacitance of only  $\sim 1.5$ pF was close to the theoretical calculation of the whole chip  $(C_{\text{chip}})$ , taking into account the estimated capacitances from both the 250  $\mu$ m sapphire substrate ( $C_{\text{sub}}$ , 1.4 pF) and the sapphire cavity ( $C_{\text{slope}}$ , 0.2 pF). This also agrees with the fact that the small membrane now contributed only minimal capacitance  $(C_m)$ . Moreover, it is also worth noting that this measured capacitance is one of the lowest values reported so far (e.g., 1.9-5.8 pF9, 0.69-1.65 pF<sup>12</sup>, 2.2 pF<sup>13</sup>, 2 pF<sup>15</sup>).

**2.7. Protein Sensing.** To validate the high-speed while the low-noise performance of the SaS nanopores, we performed

the protein nanopore sensing analysis from mid to high bandwidth. Different from DNA chains, 26 the capture rate for the globular structure protein was experimentally discovered to be 10<sup>3</sup>-10<sup>4</sup> lower than the Smoluchowski prediction,<sup>2</sup> indicating a significant loss of events. One strategy is to slow down the protein translocation, including using a salt gradient to redistribute the electric field around the nanopore regime,<sup>28</sup> applying a hydrogel buffer layer at the opening of the nanopore,<sup>29</sup> or adding ligands to the protein<sup>30,31</sup> and the nanopore to increase the pore-protein interactions.<sup>32</sup> A straightforward alternative to circumvent the modification on the chip or the protein is to increase the recording speed. However, this inevitably introduces extra noise and sacrifices the signal fidelity, especially for the conventional Si-based nanopores with high capacitive noise. Here, we used SaS nanopores to demonstrate the low-noise protein sensing as high as 250 kHz bandwidth (Figure 5a,b). A relatively big nanopore (13-14 nm) was used here to detect 93 kDa fulllength Methyl-CpG-Binding Domain Protein 1 (MBD1) protein. <sup>33</sup> Here, ~5 times lower current noise amplitude (0.2 nA) was observed for the SaS nanopore compared to the reported data detecting proteins under the same bandwidth using a conventional Si chip (1 nA at 0.5 s timescale). <sup>34</sup> In another word, the ratio of the current noise amplitude in our chip is only ~1.4% of the open-pore current (14 nA), whereas it was ~50% for a Si chip (2 nA open-pore current). This highspeed, low-noise recording serves to improve signal fidelity and makes it easier to distinguish the short (<4  $\mu$ s) and shallow events from the background noise (Figure 5e).

Comparatively, recording or filtering the signals at lower frequencies, for example, 100, 50, and 10 kHz, would have a significantly negative impact on the event rate, blockage current (Figure 5c), and dwell time (Figure 5d). For example, the event rate reduced from 2.9 Hz at 250 kHz and 100 kHz to 2.6 Hz at 50 kHz and 1.3 Hz at 10 kHz, and the blockage current (modal value) dropped significantly from 0.22 nA at 250 kHz to 0.12 nA, 0.10 nA, and 0.05 nA at 100, 50, and 10 kHz, respectively (Figure 5c). This resulted from the data loss in the signal events at a low-recording speed. Similarly, the dwelling time shifted quickly from  $\sim 4 \mu s$  at 250 kHz to 6.4  $\mu s$ , 11.1, and 62.1  $\mu$ s at 100, 50, and 10 kHz, respectively (Figure 5d). We attribute it to the data loss in the baseline close to the signal events. On the other hand, the SNR for 250 kHz (5.3) is smaller than that of 10 kHz (6.9) and 50 kHz (6.0) but higher than that of 100 kHz (4.9).

#### 3. CONCLUSIONS

In conclusion, based on our previous success to create triangular membranes on sapphire wafers using a triangular window design, we innovated hexagonal windows to further improve the fabrication uniformity and scale down the membrane dimensions. We established a method to predictably control the membrane side length  $(L_2)$  with sub-3  $\mu$ m size reproducibility and almost 100% yield. The uniform fabrication of small membranes (>80% are <30  $\mu$ m<sup>2</sup>) over a wafer scale allowed the reproducible creation of nanopore chips with a minimal chip capacitance (~1.5 pF). Such chips are useful to produce 5 times lower RMS noise current than a typical Si device, microsecond-scale protein detection under 250 kHz high bandwidth, a higher event rate, >4 times higher current blockage signals ( $\Delta I$  modal value), and minimized signal distortion compared to low bandwidths. We believe the event rates and SNRs in protein sensing can be further improved by optimizing the pore size and membrane thickness. The proposed few-micron and even sub-micron membrane fabrication approach also opened up opportunities for the integration of ultra-thin membranes (e.g., 2D materials) on sapphire for high spatial resolution and high SNR nanopore sensing (such as protein fingerprinting<sup>35</sup>).

#### 4. EXPERIMENTAL SECTION

**4.1.** Nanopore Chip Cleaning and Wetting. The nanopore chips drilled by a transmission electron microscope were cleaned with hot piranha (sulfuric acid: hydrogen peroxide = 3:1) for 10–15 min and subsequently rinsed with copious hot water. The chips were kept wet and stored in DI (deionized) water before use. The flow cell (Northern Nanopore Instruments Inc.) was put into a sealed vacuum chamber together with a Petri dish containing 4–5 droplets of trichloro(1H,1H,2H,2H-perfluorooctyl) silane (Sigma-Aldrich) overnight to improve the hydrophobicity of the channels. While a hydrophobic o-ring reservoir into the channel due to positive

capillarity,<sup>36</sup> the hydrophobic channel could improve the retention of the fluid in both the channel and the o-ring reservoir for nanopore wetting. The flow cell was then rinsed with water and fully dried with nitrogen gas. Once the chip was dried gently with nitrogen gas, it was assembled into the flow cell with o-ring sealing and silver/silver chloride (Ag/AgCl) electrodes. The salt solution was then injected into the flow cell channel to check the nanopore wettability and noise performance before injecting the biomolecule solution to collect data.

- **4.2. Nanopore Drilling.** The nanopores were drilled by a JEOL 2010F transmission electron microscope. Maximum beam current was used by switching to the largest condenser aperture and spot size. The drilling was done at the largest magnification (1.5 M) for precise nanopore size control. At 1.5 M magnification, the beam was zoomed out and held for a few minutes. The focus was re-adjusted when the beam drifted out of the focus. This holding and re-focus needed to be repeated until the beam did not drift out of focus. To drill a nanopore, the beam size was reduced to ~7 mm and rounded by tuning the condenser astigmatism. Typically, a nanopore could be fabricated on a 30 nm thick SiN membrane via 75–90 s drilling, with 7.01 kV anode A2 (focusing anode) and 3.22 kV anode A1 (extraction anode).
- **4.3. Sample Preparation.** The MBD1 protein was purchased from Abcam plc. The protein is positively charged in a pH of around 8 and has a molecular weight of 93 kDa with a GST tag (26 kDa) fused to the *N*-terminus (see Figure S19 for their estimated size, shape, and net charge). For protein sensing, the 0.03 mg/mL MBD1 protein was diluted in 1 M potassium chloride (KCl) (Sigma-Aldrich, ACS reagent) solution with 1X TE buffer to make ~20 nM MBD1 protein.
- **4.4. Protein Sensing and Data Analysis.** The protein solution was injected into the cis side of the flow cell (flow cell purchased from Northern Nanopore Instruments, Inc.) to collect the data under the filter frequency of 250 kHz using the dpatch instrument and SutterPatch software (Sutter Instrument) with a 1250 kHz sampling frequency. The flow cell was closed into a customized Faraday cage on an anti-vibration table (Nexus Breadboard, Thorlabs, Inc.) to minimize the environment noise during measurement. All the collected protein signals were then analyzed by the OpenNanopore program<sup>37</sup> to generate the dwelling time ( $\Delta t$ ) and blockade current amplitude ( $\Delta I$ ) data of each protein signal for subsequent analysis.

#### ASSOCIATED CONTENT

#### Supporting Information

The Supporting Information is available free of charge at https://pubs.acs.org/doi/10.1021/acsami.2c18983.

Membranes formed by circular window masks; hypothetical mechanism for membrane shape evolution; intersection angle calculation of n, r planes; SEM images and indices' calculation method of the sapphire facets; membrane size dependence on the mask layer; membrane area uniformity; optical images of the SiN membranes; RMS noise and PSD spectra of the nanopores; schematic and size estimation of the MBD1 protein; and measured sapphire facet slope angles and calculated indices (PDF)

#### AUTHOR INFORMATION

#### **Corresponding Author**

Chao Wang — School of Electrical, Computer and Energy Engineering, Arizona State University, Tempe, Arizona 85281, United States; Center for Photonics Innovation and Biodesign Center for Molecular Design & Biomimetics, Arizona State University, Tempe, Arizona 85281, United States; orcid.org/0000-0001-5020-961X; Email: wangch@asu.edu

#### Authors

Pengkun Xia — School of Electrical, Computer and Energy Engineering, Arizona State University, Tempe, Arizona 85281, United States; Center for Photonics Innovation and Biodesign Center for Molecular Design & Biomimetics, Arizona State University, Tempe, Arizona 85281, United States; ⊚ orcid.org/0000-0001-5097-5576

Md Ashiqur Rahman Laskar — School of Electrical, Computer and Energy Engineering, Arizona State University, Tempe, Arizona 85281, United States; Center for Photonics Innovation and Biodesign Center for Molecular Design & Biomimetics, Arizona State University, Tempe, Arizona 85281, United States

Complete contact information is available at: https://pubs.acs.org/10.1021/acsami.2c18983

#### **Funding**

This work was partially supported by the National Science Foundation (NSF) under award nos. 1847324, 1947753, 2020464, and 2027215 and by the National Institute of Health under grant no. DP2-GM149552. Access to the Arizona State University (ASU) NanoFab and/or Eyring Materials Center (EMC) was supported, in part, by NSF grant no. ECCS-1542160.

#### Notes

The authors declare no competing financial interest.

#### ACKNOWLEDGMENTS

The nanopore chips were fabricated and characterized in the NanoFab, EMC, and Solar Fab Core (SF) facilities at ASU. We thank Kenneth Mossman at ASU EMC for helping with SEM imaging, Dr. Cuifeng Ying at Nottingham Trent University for providing data analysis scripts, Dr. Md Ashif Ikbal and Dr. Rui Dai at ASU, Prof. Yang Feng at New York University, Dr. Kyle Briggs and Matthew Waugh at Northern Nanopore Instruments, Dr. Jan Dolzer and Rich Lobdill from Sutter Instrument, and Prof. Amit Meller and Dr. Yulia Marom at Technion—Israel Institute of Technology for fruitful discussions.

#### ■ REFERENCES

- (1) Xue, L.; Yamazaki, H.; Ren, R.; Wanunu, M.; Ivanov, A. P.; Edel, J. B. Solid-State Nanopore Sensors. *Nat. Rev. Mater.* **2020**, *5*, 931–951.
- (2) Fragasso, A.; Schmid, S.; Dekker, C. Comparing Current Noise in Biological and Solid-State Nanopores. *ACS Nano* **2020**, *14*, 1338–1349.
- (3) Dekker, C. Solid-State Nanopores. *Nanosci. Technol. Collect. Rev. Nat. J.* **2010**, 60–66.
- (4) Tabard-Cossa, V.; Trivedi, D.; Wiggin, M.; Jetha, N. N.; Marziali, A. Noise Analysis and Reduction in Solid-State Nanopores. *Nanotechnology* **2007**, *18*, 305505.
- (5) Hu, R.; Rodrigues, J. V.; Waduge, P.; Yamazaki, H.; Cressiot, B.; Chishti, Y.; Makowski, L.; Yu, D.; Shakhnovich, E.; Zhao, Q.; Wanunu, M. Differential Enzyme Flexibility Probed Using Solid-State Nanopores. *ACS Nano* **2018**, *12*, 4494–4502.
- (6) Venta, K.; Shemer, G.; Puster, M.; Rodríguez-Manzo, J. A.; Balan, A.; Rosenstein, J. K.; Shepard, K.; Drndić, M. Differentiation of Short, Single-Stranded DNA Homopolymers in Solid-State Nanopores. *ACS Nano* **2013**, *7*, 4629–4636.
- (7) Wanunu, M.; Dadosh, T.; Ray, V.; Jin, J.; McReynolds, L.; Drndić, M. Rapid Electronic Detection of Probe-Specific MicroRNAs Using Thin Nanopore Sensors. *Nat. Nanotechnol.* **2010**, *5*, 807–814.

- (8) Waugh, M.; Briggs, K.; Gunn, D.; Gibeault, M.; King, S.; Ingram, Q.; Jimenez, A. M.; Berryman, S.; Lomovtsev, D.; Andrzejewski, L.; Tabard-Cossa, V. Solid-State Nanopore Fabrication by Automated Controlled Breakdown. *Nat. Protoc.* **2020**, *15*, 122–143.
- (9) Balan, A.; Machielse, B.; Niedzwiecki, D.; Lin, J.; Ong, P.; Engelke, R.; Shepard, K. L.; Drndić, M. Improving Signal-to-Noise Performance for DNA Translocation in Solid-State Nanopores at MHz Bandwidths. *Nano Lett.* **2014**, *14*, 7215–7220.
- (10) Rosenstein, J. K.; Wanunu, M.; Merchant, C. A.; Drndic, M.; Shepard, K. L. Integrated Nanopore Sensing Platform with Sub-Microsecond Temporal Resolution. *Nat. Methods* **2012**, *9*, 487.
- (11) Pitchford, W. H.; Kim, H.-J.; Ivanov, A. P.; Kim, H.-M.; Yu, J.-S.; Leatherbarrow, R. J.; Albrecht, T.; Kim, K.-B.; Edel, J. B. Synchronized Optical and Electronic Detection of Biomolecules Using a Low Noise Nanopore Platform. *ACS Nano* **2015**, *9*, 1740–1748.
- (12) Balan, A.; Chien, C.-C.; Engelke, R.; Drndić, M. Suspended Solid-State Membranes on Glass Chips with Sub 1-Pf Capacitance for Biomolecule Sensing Applications. Sci. Rep. 2015, 5, 17775.
- (13) de Vreede, L. J.; Ying, C.; Houghtaling, J.; Figueiredo Da Silva, J. F.; Hall, A. R.; Lovera, A.; Mayer, M. Wafer-Scale Fabrication of Fused Silica Chips for Low-Noise Recording of Resistive Pulses through Nanopores. *Nanotechnology* **2019**, *30*, 265301.
- (14) Lee, M.-H.; Kumar, A.; Park, K.-B.; Cho, S.-Y.; Kim, H.-M.; Lim, M.-C.; Kim, Y.-R.; Kim, K.-B. A Low-Noise Solid-State Nanopore Platform Based on a Highly Insulating Substrate. *Sci. Rep.* **2014**, *4*, 7448–7.
- (15) Chien, C.-C.; Shekar, S.; Niedzwiecki, D. J.; Shepard, K. L.; Drndić, M. Single-Stranded DNA Translocation Recordings through Solid-State Nanopores on Glass Chips at 10 MHz Measurement Bandwidth. *ACS Nano* **2019**, *13*, 10545–10554.
- (16) Xia, P.; Zuo, J.; Paudel, P.; Choi, S.; Chen, X.; Rahman Laskar, M. A. R.; Bai, J.; Song, W.; Im, J.; Wang, C. Sapphire-Supported Nanopores for Low-Noise DNA Sensing. *Biosens. Bioelectron.* **2021**, 174, 112829.
- (17) Chen, Y.-C.; Lin, B.-W.; Hsu, W.-C.; Sermon Wu, Y. The Formation of Smooth Facets on Wet-Etched Patterned Sapphire Substrate. ECS J. Solid State Sci. Technol. 2014, 3, R5–R8.
- (18) Dobrovinskaya, E. R.; Lytvynov, L. A.; Pishchik, V.Properties of Sapphire. *Sapphire: Material, Manufacturing, Applications*; Springer Science & Business Media, 2009, pp 55–176.
- (19) http://www.metafysica.nl/hexagonal 6.html, May 9 2022.
- (20) Chen, Y.-C.; Hsiao, F.-C.; Lin, B.-W.; Wang, B.-M.; Wu, Y. S.; Hsu, W.-C. The Formation and the Plane Indices of Etched Facets of Wet Etching Patterned Sapphire Substrate. *J. Electrochem. Soc.* **2012**, 159, D362.
- (21) Xing, Y.; Guo, Z.; Wu, G.; Gosálvez, M. A.Characterization of Orientation-Dependent Etching Properties and Surface Morphology of Sapphire Crystal in Wet Etching. 20th International Conference on Solid-State Sensors, Actuators and Microsystems & Eurosensors XXXIII (TRANSDUCERS & EUROSENSORS XXXIII); IEEE, 2019, pp 281–284
- (22) Franssila, S.Introduction to Microfabrication, 2nd edition; John Wiley & Sons, 2010, pp 241–243.
- (23) Zhang, L.; Yuan, Z.; Jiang, S.; Shen, H.; Cao, F.; Ning, Z.; Huang, Y.; Xing, D.; Zuo, H.; Han, J.; Sun, J. Cavity Etching Evolution on the A-Plane of Sapphire Crystal in Molten KOH Etchant. J. Cryst. Growth 2020, 552, 125926.
- (24) Xing, Y.; Guo, Z.; Gosálvez, M. A.; Wu, G.; Qiu, X. Characterization of Anisotropic Wet Etching of Single-Crystal Sapphire. Sens. Actuators Phys. 2020, 303, 111667.
- (25) Shekar, S.; Niedzwiecki, D. J.; Chien, C.-C.; Ong, P.; Fleischer, D. A.; Lin, J.; Rosenstein, J. K.; Drndić, M.; Shepard, K. L. Measurement of DNA Translocation Dynamics in a Solid-State Nanopore at 100 Ns Temporal Resolution. *Nano Lett.* **2016**, *16*, 4483–4489.
- (26) Grosberg, A. Y.; Rabin, Y. DNA Capture into a Nanopore: Interplay of Diffusion and Electrohydrodynamics. *J. Chem. Phys.* **2010**, 133, 165102.

- (27) Plesa, C.; Kowalczyk, S. W.; Zinsmeester, R.; Grosberg, A. Y.; Rabin, Y.; Dekker, C. Fast Translocation of Proteins through Solid State Nanopores. *Nano Lett.* **2013**, *13*, 658–663.
- (28) Wanunu, M.; Morrison, W.; Rabin, Y.; Grosberg, A. Y.; Meller, A. Electrostatic Focusing of Unlabelled DNA into Nanoscale Pores Using a Salt Gradient. *Nat. Nanotechnol.* **2010**, *5*, 160–165.
- (29) Acharya, S.; Jiang, A.; Kuo, C.; Nazarian, R.; Li, K.; Ma, A.; Siegal, B.; Toh, C.; Schmidt, J. J. Improved Measurement of Proteins Using a Solid-State Nanopore Coupled with a Hydrogel. *ACS Sens* **2020**, *5*, 370–376.
- (30) Lu, S.-M.; Peng, Y.-Y.; Ying, Y.-L.; Long, Y.-T. Electrochemical Sensing at a Confined Space. *Anal. Chem.* **2020**, *92*, 5621–5644.
- (31) Liu, S.-C.; Ying, Y.-L.; Li, W.-H.; Wan, Y.-J.; Long, Y.-T. Snapshotting the Transient Conformations and Tracing the Multiple Pathways of Single Peptide Folding Using a Solid-State Nanopore. *Chem. Sci.* **2021**, *12*, 3282–3289.
- (32) Li, Q.; Ying, Y.-L.; Liu, S.-C.; Lin, Y.; Long, Y.-T. Detection of Single Proteins with a General Nanopore Sensor. *ACS Sens* **2019**, *4*, 1185–1189.
- (33) https://www.uniprot.org/uniprot/Q9UIS9, 13 June 2022.
- (34) Larkin, J.; Henley, R. Y.; Muthukumar, M.; Rosenstein, J. K.; Wanunu, M. High-Bandwidth Protein Analysis Using Solid-State Nanopores. *Biophys. J.* **2014**, *106*, 696–704.
- (35) Afshar Bakshloo, M.; Kasianowicz, J. J.; Pastoriza-Gallego, M.; Mathé, J.; Daniel, R.; Piguet, F.; Oukhaled, A. Nanopore-Based Protein Identification. *J. Am. Chem. Soc.* **2022**, *144*, 2716–2725.
- (36) McNeely, M. R.; Spute, M. K.; Tusneem, N. A.; Oliphant, A. R. Hydrophobic Microfluidics. Microfluidic Devices and Systems II. SPIE1999, vol 3877, pp 210–220.
- (37) Raillon, C.; Granjon, P.; Graf, M.; Steinbock, L. J.; Radenovic, A. Fast and Automatic Processing of Multi-Level Events in Nanopore Translocation Experiments. *Nanoscale* **2012**, *4*, 4916–4924.

### ☐ Recommended by ACS

# Ultrathin, High-Lifetime Silicon Nitride Membranes for Nanopore Sensing

Shankar Dutt, Patrick Kluth, et al.

MARCH 17, 2023

ANALYTICAL CHEMISTRY

READ 🗹

## **Evaluation of Nanopore Sensor Design Using Electrical and Optical Analyses**

Lauren A. Mayse, Liviu Movileanu, et al.

JUNE 01, 2023

ACS NANO

READ 🗹

# Highly Rectifying Conical Nanopores in Amorphous ${\rm SiO_2}$ Membranes for Nanofluidic Osmotic Power Generation and Electroosmotic Pumps

Alexander Kiy, Patrick Kluth, et al.

MAY 09, 2023

ACS APPLIED NANO MATERIALS

RFAD **[**✓

# Glass Capillary-Based Nanopores for Single Molecule/Single Cell Detection

Xin Guan, Yongdong Jin, et al.

JANUARY 20, 2023

ACS SENSORS

READ 🗹

Get More Suggestions >